1 **Title: The structural basis for regulation of the glutathione transporter Ycf1 by regulatory**
2 **domain phosphorylation**

3 **Authors:** Nitesh Kumar Khandelwal[1], Cinthia R. Millan[1], Samantha I. Zangari[1], Samantha Avila[2#],
4 Dewight Williams[3], Tarjani M. Thaker[1], Thomas M. Tomasiak[1]*

5 **Affiliations:**

6 [1]Department of Chemistry and Biochemistry, University of Arizona; Tucson, AZ 85721

7 [2]Department of Biochemistry and Biophysics, University of California – San Francisco, San
8 Francisco CA, 94158

9 #Present address – Duke University School of Medicine, Durham, NC, 27710

10 [3]Eyring Materials Center, Arizona State University; Tempe, AZ 85287

11 *Corresponding author. Email: tomasiak@arizona.edu

12

13 **Abstract**
14 Yeast Cadmium Factor-1 (Ycf1) sequesters heavy metals and glutathione into the vacuole to
15 counter cell stress. Ycf1 belongs to the ATP binding cassette C-subfamily (ABCC) of transporters,
16 many of which are regulated by phosphorylation on intrinsically disordered domains. The
17 regulatory mechanism of phosphorylation is still poorly understood. Here, we report two cryo-EM
18 structures of Ycf1 at 3.4Å and 4.0Å in distinct inward-facing open conformations capturing a
19 previously unobserved ordered state of the intrinsically disordered regulatory domain (R-domain).
20 R-domain phosphorylation is clearly evident and induces a topology promoting electrostatic and
21 hydrophobic interactions with Nucleotide Binding Domain 1 (NBD1) and the lasso domain. These
22 interactions stay constant between the structures and are related by rigid body movements of the
23 NBD1/R-domain complex. Biochemical data further show R-domain phosphorylation reorganizes
24 the Ycf1 architecture and is required for maximal ATPase activity. Together, we provide long-
25 sought after insights into how R-domains control ABCC transporter activity.

26

27

28 **Introduction**

29   ATP-binding cassette (ABC) transporters regulate the movement of diverse molecules to
30 support fundamental roles of the membrane including lipid homeostasis, ion transport, and
31 detoxification. The Yeast Cadmium Factor 1 (Ycf1) performs a similar protective function by
32 transporting the tripeptide glutathione, which is the main non-protein thiol in cells, upon oxidation
33 to maintain redox balance or after conjugation to toxic heavy metals such as cadmium, mercury,
34 or lead into vacuoles[1–5]. These metals make up three of the top ten environmental toxins as
35 defined by the CDC (#s 1,3, and 7 - https://www.atsdr.cdc.gov/spl/index.html#2019spl), marking
36 Ycf1 as an attractive bioremediation target. Ycf1 also acts as a major redox sink and regulates
37 redox levels in cytoplasm by sequestering glutathione after it is oxidized. In this way, Ycf1 serves
38 a powerful protective function against metals and ROS, both of which are electrophiles that attack
39 DNA, proteins, and the cell membrane.

40   Because of their essential roles in responding to cell stress, such proteins are often tightly
41 regulated. Protein phosphorylation represents one such mechanism by which protein and
42 transporter function can be tuned for specific cellular contexts. In general, approximately half of
43 all human ABC transporters are phosphorylated[6] including the medically important P-

44 glycoprotein[7], the Sulfonyl Urea Receptor (SUR1[8]), and the Cystic Fibrosis Transmembrane
45 Conductance Regulator (CFTR[9]). Rapid regulation is especially important to the C-subfamily of
46 ABC transporters (ABCC family), which includes Ycf1 and CFTR, in particular because of their
47 roles in regulating osmotic balance, neutralizing reactive oxygen species, or combating the effects
48 of antifungal or anticancer agents in many organisms. Often, transporter phosphoregulation is
49 mediated through phosphorylation on regions outside of the highly structurally conserved
50 transport machinery. Instead, phosphorylation sites arise in long, disordered loops between
51 domains or at the termini. In ABCC transporters, such regulatory elements are evolutionary
52 additions to the canonical ABC exporter fold composed of two transmembrane domains (TMDs)
53 and two nucleotide binding domains (NBDs) (**Fig. 1A**). These additions include an accessory
54 TMD called TMD0, a Lasso domain that connects TMD0 and TMD1, and a ~60-140 amino acid
55 disordered domain termed the regulatory domain (R-domain) that connects NBD1 and TMD2[10–
56 13]. The R-domain in particular acts as a signaling and interaction hub in ABCC transporters and
57 contains multiple PKA, PKC, and CKII recognitions sites with otherwise little sequence
58 conservation.

59 Disruption of this regulatory function can have profound cellular effects. Mutations of R-
60 domain phosphorylation sites lead to loss of cadmium tolerance in Ycf1[11] and to lower open
61 probability (but not overall open duration) and sensitivity to ATP concentration in the Ycf1 homolog
62 CFTR[14,15]. Furthermore, mutations in 19 of the total ~130 residues of the CFTR R-domain are
63 associated with mutants in the CFTR-linked lung disease, cystic fibrosis (www.cftr2.org).
64 Phosphorylation can induce negative regulation as well, particularly on the lasso domain in both
65 Ycf1[16] and the Ycf1 functional homolog Multidrug Resistance Protein 1 (MRP1[17]). Finally, the R-
66 domain provides a surface for protein-protein interactions, including to other transporters such as
67 SLC26A3 and the adapter proteins 14-3-3β[18].

68 Despite recent advances in ABC transporter structural biology using cryo-electron
69 microscopy (cryo-EM), the biophysical basis of these diverse R-domain interactions is poorly
70 understood. Barriers to these characterizations hinge on the nature of the R-domain, which is
71 predicted to be unstructured based on low sequence conservation[19] and experimentally confirmed
72 with circular dichroism (CD)[19,20] and proteolysis analysis that estimate as low as 5% helical
73 content[20]. However, more recent NMR experiments point to discrete helical fragments in the R-
74 domain and direct interactions with NBD1[21]. Meanwhile, cryo-EM structures of ABCC1,CFTR, and
75 Ycf1 reveal a mostly disordered R-domain[22–24] without assigned sequence for the phosphorylation
76 sites, limiting our understanding of R-domain interactions. Structures of human CFTR (hCFTR)
77 and Ycf1 have revealed density for segments of the R-domain in proximity to NBD1[25].
78 Unfortunately, the lack of R-domain sequence assignment in these models prohibits insights into
79 the precise interacting regions[25] and to date no structure of an intact R-domain with the NBDs has
80 been determined in any state.

81 In this study, we have used cryo-EM to determine the 3.4Å and 4.0Å resolution structures
82 of endogenously phosphorylated *Saccharomyces cerevisiae* Ycf1 in two inward-facing
83 conformations: wide (IFwide) and narrow (IFnarrow). We observe a resolved section of the R-
84 domain that is most highly conserved in the ABCC family and includes the phosphorylation sites
85 (**Fig. 1B-C; Supplementary Table S1**). Our structures reveal the extensive interaction interface
86 between the phosphorylated R-domain, NBD1, and the lasso-domain. Interestingly, the networks
87 we observe are nearly constant between the two states, related only by a rigid movement of the
88 entire R-domain/NBD1 complex relative to NBD2, with very minor changes in the positioning of
89 the R-domain along NBD1. Biochemical investigation shows that phosphorylation induces
90 changes in ATPase activity at the same time as it causes structural changes. Thus, we provide
91 the structural and biochemical details of phosphorylation-dependent regulation of Ycf1.

92

Results

Cryo-EM structures of inward-facing wide and narrow states of Ycf1

In asymmetric ABC transporters, like Ycf1, only one of two NBDs (NBD2) is capable of efficient ATP hydrolysis. To enable structural studies of Ycf1 we expressed and purified two forms the *S. cerevisiae* DSY5 strain: wild-type (WT) and the NBD2 Walker B mutant E1435Q (**Fig. S1**). Grids of both WT and E1435Q Ycf1 in apo conditions were prepared as described in the methods, but only the E1435Q Ycf1 dataset yielded homogenous particles from which we successfully identified not one but two inward-facing conformations determined to 3.4Å and 4.0Å resolution (**Fig. 1A-C**). The E1435Q mutant resulted in substantially lowered ATPase activity compared to WT Ycf1 (Vmax 18633 ± 474.7 nmol/sec/mg) (**Fig 1D**), likely allowing the trapping of these conformations. Both maps were sufficiently detailed to enable modeling of an almost complete Ycf1 protein structure. The features we observe are largely consistent with other ABCC structures [26–28]. This includes 17 transmembrane helices of TMD1 and TMD2, the accessory transmembrane domain TMD0 unique to the ABCC family, the lasso motif, both NBDs, and surprisingly a major portion of a previously uncharacterized region of the R-domain (**Fig. 1A-C**).

The two states are defined by a clear differences in the interdomain distances between the NBDs (**Fig. 1B and C**) and the TMDs that define the substrate binding cavity (**Fig. 1E**). We designated the state in which the NBDs are further apart as IFwide (**Fig. 1B**) and the state in which the NBDs are closer as IFnarrow (**Fig. 1C**). The unoccluded substrate cavities in both structures are large enough to accommodate oxidized glutathione (GSSG) (**Fig. 1E**) previously shown to be a primary physiological substrate in cells[29]. These results are consistent with our ATPase data that show GSSG indeed stimulates ATPase activity at physiologically relevant concentrations (µM concentration range) (**Fig. 1F; Fig. S1E**).

The Ycf1 R-domain is in a phosphorylated state with an ordered regulatory domain

The most striking findings of our structures are the visualization of every regulatory element, including the R-domain (residues 901-935) phosphorylated in three positions. The R-domain is helical (residues 920-929) in the C-terminal segment and lacks secondary structure (residues 901-919 and 930-935) in the other. The C-terminal helix was key to sequence assignment and aligns with partial models from CFTR cryo-EM structures (**Fig. S7A-E,**[25]), with helical NMR assignments in CFTR[21], and with evolutionary coupling analysis of co-evolving residues[30] from a multisequence alignment of 13,723 homologs (**Fig. S7E**). The R-domain encircles NBD1 in both IFwide and IFnarrow (**Fig. 1B-C**) and is stabilized by extensive contacts along a basic groove of the NBD1 perimeter, intracellular loop 4, and the lasso domain (**Fig. 2A-D; Fig. 3**). This positioning differs from the positioning and sequence assignment of short, discontinuous R-domain fragments in a previous Ycf1 structure[28].

The R-domain houses several phosphorylation motifs shown to be important for regulation. We assigned phosphorylation to S908, T911, and S914 in our model based on pronounced additional electron potential density at these residues (**Fig. 2E**). Mass spectrometry and phosphostaining analysis confirm phosphorylation at these three sites in both WT and E1435Q Ycf1 (**Fig. 2F; Table S2**). These phosphates make extensive contacts with the Nϵ and Nη atoms in the guanidyl groups of R716 on NBD1 and R206 on the lasso domain in proximity to be either hydrogen-bonding or a strong charge-charge interactions (**Fig. 2D**). Among the phosphosites, S908 is part of a recognition motif for PKA-like kinases called the RRAS motif (or dibasic consensus sequence) and displays a similar conformation to that of a phosphomimetic peptide bound to PKA (PDB ID: 1ATP[31]). T911 also serves as part of a CKII kinase recognition motif (S/T-(x)$_n$-S/T) that partially overlaps with the PKA-like kinase site (**Fig. 2B**). Overall, the resolvable range of the Ycf1 R-domain coincides with the region containing the highest sequence conservation to CFTR, which possesses a longer R-domain than Ycf1 but otherwise conserved kinase motifs (**Fig. 2B, Fig. S7E**).

Phosphorylation of the R-domain controls dynamics and ATPase activity

The R-domain interaction with NBD1, TMDs, and lasso motif has been hypothesized to be highly dynamic and dependent on phosphorylation of the R-domain. To interrogate this effect on our reconstituted sample, we prepared dephosphorylated Ycf1 by treating it with lambda phosphatase (**Fig. 2F**) and subjecting the sample to limited proteolysis with trypsin. We observed that dephosphorylated Ycf1 substantially changes the digestion pattern in comparison to endogenously phosphorylated Ycf1(**Fig. 2G**), with a clear increase to protease accessibility in the dephosphorylated state as judged by a more complete digestion (ie loss of intermediate sized bands) in the dephosphorylated state. We reasoned that this was due to changes in the R-domain position or conformation in a phosphorylation dependent manner similar to CFTR[25] but note that the phosphates themselves may block protease accessibility to some sites as well.

To investigate the functional impact of these structural changes due to dephosphorylation, we interrogated changes in ATPase activity. ATPase assays show a drastic activity reduction in dephosphorylated Ycf1 (**Fig. 2H**), suggesting that the interactions of phosphorylated S908, T911, and S914 are major drivers of an architecture that facilitates ATP hydrolysis. This is consistent with cell viability data from *S. cerevisiae* cells where S908 and T911 Ycf1 mutants show deficient cadmium detoxification, resulting in cell death[11].

Tightly embedded hydrophobic surfaces stabilize the R-domain NBD interaction

Together, the phosphorylation sites form a scaffold that engages NBD1 and the lasso motif along a single axis to connect NBD1 and the TMDs (**Fig. 3A**). The electrostatic interactions are supported by a substantial burying of hydrophobic surfaces at 3 sites (site 1: I621 - L802 - I902 - I904 (**Fig. 3B**); site 2: L912 - I915 - I1154 (**Fig. 3C**); and site 3: F917 - I1123 - L1120 (**Fig. 3D**)). These interactions are poised to provide a large thermodynamic driving force of R-domain binding and stabilize the R-domain/NBD1 interface, burying ~1530 $Å^2$ and ~1338 $Å^2$ of surface area along the entire R-domain in IFnarrow and IFwide, respectively (~523$Å^2$ (IFnarrow) and ~480$Å^2$ (IFwide) specifically between NBD1 and the R-domain) (**Fig. 2C**). In addition, this region overlaps with known allosteric motifs, including the x-loop and the GRD motif, both of which also contact each other in IFnarrow (**Fig. 3E**).

Location of an inhibitory phosphosite at S251 in proximity to R-domain phosphosites

The lasso domain region adjacent to the R-domain also contains a conserved phosphorylation site that negatively regulates transport, S251 (T249 in the Ycf1 homolog MRP1)[16,17]. Though we do not observe phosphorylation in our structure at this position, S251 is accessible to the surface and poised to disrupt R-domain interactions through electrostatic repulsion of phosphate groups in the R-domain (**Fig. 2D**). Thus, our structures provide a plausible explanation of the negative impact of the lasso domain phosphorylation on Ycf1 function.

The two structures of Ycf1 show different NBD orientation with a single-occluded ATP site in IFnarrow

These observed R-domain - NBD1 - lasso contacts are consistent between IFwide and IFnarrow with minimal changes between these domains (**Fig. 4A**). Instead, a rearrangement within the R-domain correlates with overall movements in the structure, including a change in angle between residues G913, G918 and G932 of the R-domain from 130º (IFwide) to 137.5º (IFnarrow) (**Fig. 4B**). The glycines G918 and G932 cap the helical R-domain region and act as a hinge for the movement of this structured region between the transition from IFwide to IFnarrow.

In contrast to the interaction sites themselves, the major structural consequences of the IFwide to IFnarrow transition are induced at the ATP binding sites. These sites not only move closer in IFnarrow but also rotate to occlude the non-functional ATP binding site in NBD1 (**Fig. 4C**). Notably, the second site in NBD2 (active) is open for ATP binding. NBD2 is the less ordered of the two NBDs as inferred from relatively weaker cryo-EM density in this region in both states.

191 This disorder is a predominant feature also noted for a third, less well-resolved state that we call
192 IFtransition (**Fig. S3C**) which was insufficiently detailed to enable model building. Concurrently,
193 several coupling elements that connect the NBDs and TMDs, including the NBD1 X-loop and
194 GRD motif[32], are brought into contact upon transition to IFnarrow (**Fig. 3E**). Overall, these
195 architectural changes resemble changes in substrate-bound and substrate-free states of MRP1
196 (**Fig. S8A-F**)[27,33] and point to a model where Ycf1 R-domain phosphorylation helps stabilize NBD1
197 to recruit other domains into a conformation (IFnarrow) suitable for ATP binding and initiation of
198 transport. We propose this yields a primed, active state ready for transport.
199
200
201 **Discussion**

202 The structures of Ycf1 determined here reveal previously unobserved insights in the ABCC
203 family of ABC transporters that inform on how they are regulated. This includes an inward-open
204 conformation with an intact and endogenously phosphorylated R-domain tightly bound to NBD1.
205 This provides a more complete model than previous ABCC structures, which resolve small
206 fragments of the R-domain, do not resolve the phosphorylation sites, and do not assign the
207 sequence[28,34,35]. The presence of an ordered R-domain position poses a surprise, since many
208 alternate models exist for the R-domain mechanism including a model where it is completely
209 disordered or where it resides only between NBD1 and NBD2 in a semi-ordered state.

210 The findings in this work support decades of biochemical, cellular, and clinical data on the
211 consequences of R-domain interactions. The multiple phosphate binding interactions to a
212 common surface along NBD1 and the lasso domain explain the well-known robustness to loss of
213 any single phosphorylation site on the R-domain[9,11] and the requirement for an intact N-terminus
214 containing the lasso domain of Ycf1 for activity[36]. The extensive R-domain and NBD1 interactions
215 increase the ATPase rate in a manner consistent with CFTR, where R-domain phosphorylation
216 potentiates ATP binding and hydrolysis but otherwise does not induce activity alone[37]. Our
217 structures also are consistent with the visible R-domain density in CFTR and polyalanine models
218 built into this density (**Fig. S7A-D**).

219 The position of the R-domain informs on the phosphorylation activation mechanism and
220 provides clarification on the competing models that exist. In the most widely held model, CFTR
221 activation is proposed to depend on release of the R-domain positioned between NBD1 and NBD2
222 upon phosphorylation, which induces a completely unbound and disordered state[26]. Our findings
223 here do not support this model. Instead, our results suggest that the extensive interactions
224 between the phosphorylated R-domain and the rest of Ycf1 represent a stimulatory R-domain
225 architecture. However, our structures do not rule out an inhibitory role for the unphosphorylated
226 state (**Fig. 4D**). Based on our functional data, we propose a model where the R-domain transitions
227 from unbound/disordered to bound/ordered upon phosphorylation, residing either between the
228 NBDs when dephosphorylated[38] or near NBD1 but loosely associated. Phosphorylation along the
229 R-domain drives association with the periphery of NBD1 (**Fig. 2C**) that is reflected as both
230 increased ATPase activity and R-domain stability (**Fig. 2G-H**). The clustering of the R-domain
231 and lasso domain also provides a plausible explanation for the inhibitory role of S251
232 phosphorylation, which is poised to disrupt the R-domain interaction network by charge repulsion
233 (IFwide inhibited - **Fig. 4D**). In conclusion, R-domain interactions lend a regulatory effect
234 analogous to that of a transmission "clutch" that only engages a motor but otherwise does not
235 perform work itself.

236 These results also rationalize key clinically relevant findings related to other ABCC family
237 members. The extensive electrostatic, hydrogen bonding, and hydrophobic interactions on the R-
238 domain explain how mutations distal from phosphorylation sites may nevertheless contribute to
239 dysfunction. Additionally, the site equivalent to the most widespread cystic fibrosis linked mutant

240 (CFTR delF506), Ycf1 F713, is located in NBD1 directly adjacent to the phosphorylation sites of
241 the R-domain and is coordinated by cation-pi interactions with two conserved arginine side chains,
242 R765 and R1150 (**Fig. S7H**). Finally, the binding site of lumacaftor, a clinically used corrector that
243 stabilizes unfolded CFTR, binds in the outer perimeter of NBD1 near the R-domain binding site
244 [39]. The high convergence of several important effects near one region where the R-domain, NBD1,
245 and lasso domain come together suggest the general importance of the R-domain interactions
246 observed in our structures.

247   In summary, our structures provide mechanistic insights about post-translational
248 modification (phosphorylation) on an important class of transporters, the ABCC family. The
249 presence of a single defined binding site for the conserved part of the R-domain confirms an
250 anticipated but elusive binding site and may provide implications for several other types of
251 transporters where such long phosphorylated unstructured domains or loops are widespread.
252 Such a defined binding site could also provide a basis for allosteric modulation of transporter
253 function in a diverse array of settings.

254

255 **Methods**

256 **Cloning, expression, and purification**

257   The *S. cerevisiae YCF1* (Yeast Cadmium Factor 1) gene was codon-optimized and cloned
258 into the p423_GAL1 yeast expression vector as an N-terminal Flag (DYKDDDDK) and C-terminal
259 decahistidine (10X His) tagged fusion protein (GenScript) (**Fig. S1A**). The E1435Q mutant was
260 generated by site-directed mutagenesis (forward primer: 5'-
261 CTTGGTTTTGGATCAAGCTACAGCTGCAG-3'; reverse primer 5'-
262 CTGCAGCTGTAGCTTGATCCAAAACCAAG-3') and verified by sequencing (Elim
263 Biopharmaceuticals, Inc).

264   For protein expression, the *S. cerevisiae* strain DSY-5[40] (Genotype MATa leu2 trp1 ura3-
265 52 his3 pep4 prb1) was transformed with the Ycf1 expression construct and a 50 mL primary
266 culture grown for 24 hours at 30°C with shaking at 200 rpm in SC-His media (0.67% w/v yeast
267 nitrogen base without amino acids, 2% w/v glucose, and 0.08% w/v amino acid dropout mix
268 without histidine). A secondary 750 mL culture of SC-His media was inoculated with 2% of the
269 primary culture (15 mL) and grown under the same growth conditions for an additional 24 hours
270 prior to induction by adding YPG media (1% w/v yeast extract, 1.5% w/v peptone, and 2% w/v
271 galactose final concentration) from a 4X YPG media stock. The culture was grown for an
272 additional 16 hours at 30°C prior to harvesting by centrifugation at 5000xg for 30 minutes at 4°C.

273   For protein purification, harvested cells were resuspended with ice-cold lysis buffer (50
274 mM Tris-Cl pH 8.0, 300 mM NaCl, and cOmplete, EDTA-free protease inhibitor cocktail tablets
275 (Roche)) at a ratio of 3.2 mL/g of cell pellet. Resuspended cells were lysed on ice by bead beating
276 with 0.5 mm glass beads for 8 cycles consisting of 45 seconds of beating, with 5 minutes between
277 cycles. Lysates were collected by vacuum filtration through a coffee filter and membranes
278 harvested by ultracentrifugation at 112,967xg for 1.5 hours prior to storage at -80°C. Membranes
279 were solubilized in resuspension buffer (50 mM Tris-Cl pH 7.0, 300 mM NaCl, 0.5% 2,2-
280 didecylpropane-1,3-bis-β-D-maltopyranoside (LMNG)/0.05% cholesteryl hemisuccinate (CHS)
281 supplemented with protease inhibitor as described above) at a ratio of 15 mL/g of membrane at
282 4°C for 4 hours. Solubilized membranes were clarified by centrifugation at 34,155xg for 30 min at
283 4°C. The clarified supernatant was filtered through a 0.4 µM filter to remove the insoluble fraction
284 and supplemented with 30 mM Imidazole pH 7.0 immediately before loading at a flow rate of 2
285 mL/min onto a 5 mL Ni-NTA immobilized metal affinity chromatography (IMAC) column (Bio-Rad)
286 equilibrated in Buffer A (50 mM Tris-Cl, 300 mM NaCl, 0.01% LMNG/0.001% CHS, pH 7.0).

287 Following loading, the column was washed with 10 column volumes (CV) of Buffer A to remove
288 nonspecifically bound proteins then followed by a gradient of Buffer B (50 mM Tris-Cl, 300 mM
289 NaCl, 500 mM Imidazole 0.01% LMNG/0.001% CHS, pH 7.0) consisting of the following step
290 sizes: 6% (10CV), 10% (2CV), 16% (2 CV), and 24% (2CV). Protein was eluted with 4CV of 60%
291 buffer B and immediately diluted 10-fold with Buffer A prior to concentration and 3 rounds of buffer
292 exchange to remove excess imidazole by centrifugation at 4000 rpm at 4°C in 100 kDa cutoff
293 concentrators (Amicon). Concentrated, buffer exchanged sample was lastly purified by size
294 exclusion chromatography (SEC) at 4°C by injecting sample onto a Superose 6 Increase 10/300
295 GL column (GE Healthcare) equilibrated in SEC buffer (50 mM Tris, 300 mM NaCl, pH 7.0)
296 supplemented with either 0.01% LMNG/0.001%CHS or 0.06% digitonin and immediately used for
297 biochemical assay or cryo-EM grid preparation following quantification by BCA Assay (Pierce).

298

Cryo-EM grid preparation and data acquisition

300   Cryo-EM grids for wild-type (WT) and E1435Q Ycf1 were similarly prepared. Immediately
301 following SEC purification, 5 µL of concentrated WT (15.2 mg/mL) or E1435Q (5.94 mg/mL) Ycf1
302 sample was applied to a CFlat-1.2/1.3-4C-T (WT Ycf1) or QF-1.2/1.3-4Au grid (E1435Q Ycf1)
303 purchased from Electron Microscopy Sciences. Grids were placed inside of a Leica EM GP2
304 equilibrated to 10ºC and 80% humidity. Following a 10s incubation, the side of the grid to which
305 sample was applied was blotted on Whatman 1 paper (8s for WT; 3.5s for E1435Q), then
306 immediately plunge frozen in liquid ethane equilibrated to -185ºC. A total of 3,262 movies were
307 captured for WT Ycf1 using Serial EM software on a Titan Krios at 300 kV equipped with a K2
308 Summit detector (Gatan) at Arizona State University (ASU). For E1435Q, 8,499 movies were
309 captured on a Titan Krios at 300 kV equipped with a K3 Summit detector (Gatan) at the Pacific
310 Northwest Center for Cryo-EM (PNCC). Movies of both WT and E1435Q Ycf1 samples were
311 collected at 22,500X magnification with automated super resolution mode and defocus ranges of
312 -0.5-2.8 µm (WT Ycf1) and -0.9 to -2.1 µm (E1435Q Ycf1). Movie frames for WT Ycf1 contained
313 40 frames with a per frame exposure of 1.4 electrons /Å^2 (~56 electrons /Å^2 total dose). Movies
314 of E1435Q Ycf1 contained 60 frames with a per frame exposure of 0.9 electrons /Å^2 dose rate
315 (~54 electrons /Å^2 total dose).

316

Cryo-EM data processing

318   The Ycf1 E1435Q dataset was processed in RELION (3.0 and 3.1)[41] and cisTEM[42]. Drift
319 correction was performed using MotionCor2[43] to generate an image stack with a pixel size of
320 1.031 Å/pixel. The contrast transfer function (CTF) was estimated for dose-weighted micrographs
321 using CTFFIND4.1 prior to particle picking using a reconstruction of WT Ycf1 (**Fig. S2**)[44]. Manual
322 particle picking was performed on a subset of micrographs belonging to the WT Ycf1 dataset and
323 subject to reference free 2D Classification to generate references for automated particle picking.
324 Following ab-initio 3D map generation and several rounds of 3D classification and 3D refinement
325 in RELION, a ~6.0 Å resolution map of WT Ycf1 was obtained (**Fig. S2**), low-pass filtered to 20Å
326 resolution, and used as a reference for automatic particle picking in RELION in the E1435Q
327 mutant dataset using a 15º degree angular search (**Fig. S3**). A total 2,159,582 particles were
328 automatically picked, extracted with 4X binning resulting in a box size of 440 pixels with 4.124
329 Å/pixel. Multiple rounds of 2D classification were performed to remove bad particles resulting in
330 1,626,297 particles subject to 3D analysis in RELION following extraction with 2X binning and a
331 box size of 300 pixels with 2.062 Å/pixel. The two major classes corresponding to two distinct
332 states from the second round of 3D Classification were extracted with a 300 pixel box size at the
333 full pixel size of 1.031 Å/pixel and subjected to iterative rounds of CTF refinement, Bayesian
334 polishing, and postprocessing in RELION. To reduce alignment bias due to the presence of the

335 detergent micelle, SIDESPLITTER refinement[45] was implemented in later stages of 3D
336 Refinement in RELION. A final round of alignment-free 3D Classification to remove structural
337 heterogeneity revealed the IFnarrow and IFwide states, as well as a third state (IFtransition) in
338 which NBD2 was poorly resolved. Maps from RELION were further refined in cisTEM and used
339 for manual model building. ResMap was used for local resolution estimation performed on cisTEM
340 maps [46]. A summary of the data processing workflow and final EM map quality is reported in **Figs.**
341 **S2-5**.

342

Model building and refinement

344 An initial model of Ycf1 was built using the SWISS-MODEL server[47] and 6jb1 as a
345 template[48]. Manual model building was performed in COOT[49]. Iterative cycles of real-space
346 refinement and analysis were performed in Phenix[50] and CCP-EM modules[51,52] were used
347 throughout the structure building process for map sharpening/blurring and for structure analysis.
348 Secondary structure restraints were used extensively, and model building was guided by
349 evolutionary couplings analysis (**Fig. 7F-G**). Modrefiner was used in the early stages of refinement
350 to help assign secondary structure and correct geometry[53]. Isolde was used to optimize model to
351 map fit and to improve geometry[54]. Molprobity was used extensively through Phenix and through
352 a dedicated web service to optimize geometry[55]. To maintain proper geometry, starting model
353 restraints and harmonic restraints were used extensively in Phenix. Analysis of the Ycf1 substrate
354 binding cavity volume was performed using the 3V server[56]. In this calculation, the Ycf1 NBDs
355 were excluded in order to obtain information restricted to cavity volumes in the TMDs. A probe
356 size of 2.5Å was used as was previously used in assessment of a bacterial glutathione
357 transporter[57].

358

Evolutionary coupling analysis of Ycf1

360 Evolutionary couplings analysis was performed using the Evcouplings package
361 downloaded from https://github.com/debbiemarkslab/EVcouplings. Sequences were chosen
362 automatically from the JackHMMR[58] protocol supplied with the Evcouplings suite using the
363 Uniref90 database. A total of 13,723 sequences were identified and coupling scores calculated
364 with PLMC[30]. HH-suite was used to cluster similar sequences at an 80% cutoff that would
365 otherwise skew the distribution of homologs[59]. Scores with a cutoff probability of ≥0.99% were
366 used to identify positive interactions.

367

ATPase activity assays

369 For evaluating ATPase activity, WT and E1435Q Ycf1 were expressed and purified as
370 described above in buffer containing 0.01% LMNG and 0.001% CHS. ATPase rates were
371 determined at 30ºC using an enzyme-coupled assay previously described with slight
372 modification[60]. Each reaction consisted of 75 µL volumes containing 6.45 µg of protein in a
373 reaction mix of 20 mM Tris-HCl pH 7.0, 10 mM $MgCl_2$, 1 mM PEP, 55.7 / 78.03 U/mL PK/LDH,
374 0.3 mg/mL NADH and ATP at varying concentrations. Following the addition of ATP, the initial
375 rate of NADH consumption was monitored by measuring the absorbance every minute at 340 nM
376 for 30-45 min on a Synergy Neo2 Multi-mode Microplate Reader (BioTek). Nonlinear regression
377 analysis of data fit with the Michaelis-Menten equation in GraphPad Prism 9 was used to generate
378 kinetic parameters for at least three technical replicates.

379 Substrate-stimulated ATPase activity was measured as described above and in the
380 presence of varying concentrations of oxidized glutathione (GSSG) (**Fig. 1F; Fig. S1E)**. The

381 concentration of ATP in these experiments was held constant at 1 mM. Data for the basal ATPase
382 activity in the absence of GSSG was subtracted from the substrate-stimulated data prior to fitting,
383 as was performed in the study of ABCG2[61]. Data were fit using nonlinear regression in GraphPad
384 Prism 9 to derive EC50 and Vmax values.

385

Characterization of Ycf1 phosphorylation

387 Ycf1 phosphorylation was assayed by in-gel phosphoprotein staining. Dephosphorylated
388 Ycf1 for these experiments was generated by treating SEC-purified Ycf1 with Lambda
389 phosphatase (Lambda PP, NEB) for 45 min at 4°C as previously described for CFTR[26]. Following
390 phosphatase treatment, dephosphorylated Ycf1was subject to a second round of SEC purification
391 to remove excess enzyme immediately prior to use for subsequent biochemical analysis. For in
392 gel phosphoprotein staining, equal quantities (5 ug) of untreated Ycf1 and lambda PP (NEB)
393 treated samples were separated on two separate 10% SDS- PAGE gels, one of which was then
394 stained with Pro-Q Diamond Phosphoprotein Gel Stain (Thermo Scientific) following the
395 manufacture's protocol to detect protein phosphorylation. The second gel was simultaneously
396 stained with Coomassie Brilliant Blue R-250 as a control for monitoring total protein levels.

397

LC-MS/MS analysis of phosphorylated Ycf1

399 To measure quantitative phosphorylation of purified Ycf1, 10 µg of WT Ycf1 or E1435Q
400 were Trypsin/LysC (Promega, Madison WI) digested with an S-Trap column (ProtiFi, Farmingdale
401 NY) using the manufacturer's suggested protocol following reduction with DTT and alkylation with
402 IAA with ProteaseMax (0.1% Promega) added to the digestions. The LC-MS/MS analysis was
403 performed using a Q-Exactive Plus (Thermo Fisher Scientific, San Jose, CA) mass spectrometry
404 with an EASY-Spray nanoESI. Peptides were separated using an Acclaim Pepmap 100 trap
405 colum (75 micron ID x 2cm from Themo Scientific) and eluted onto an Acclaim PepMap RSKC
406 analytical column (75 micron ID x 2cm, Thermo Scientific) with a gradient of solvent A (water and
407 0.1% formic acid) and solvent B (acetonitrile and 0.1% formic acid). The gradients were applied
408 starting with 3-35% Solvent B over 90 minutes, then 25 to 50% solvent B over 20 minutes, 50-
409 95% solvent B over 5 minutes, and a 100% solvent B for 10 min, and then 3% solvent B for 10
410 min.

411 Data were collected with a flow rate of 300 nL/min applied with a Dionex Ultimate 3000
412 RSLCnano system (Thermo Scientific) with data dependent scanning using Xcalibur v
413 4.0.27.19[62]. A survey scan at 70,000 resolution scanning mass/charge (m/z) 350-1600 with an
414 automatic gain control (AGC) target of $1e^6$ with a maximum injection time (IT) of 65msec, then a
415 high-energy collisional dissociation (HCD) tandem mass spectrometry (MS/MS) at 37 NCE
416 (normalized collision energy) of the 11 highest intensity ions at 17,5000 resolution, 1.5m/z
417 isolation width, $5e^4$ AGC, and 65msec maximum IT. Dynamic exclusion was used to select an m/z
418 exclusion list for 30 sec after single MS/MS and ions with a charge state of +1, 7, >7, unassigned,
419 and isotopes were excluded.

420 Search of MS and MS/MS data were performed against the Ycf1-E1435Q sequence, the
421 Uniprot *S. cerevisiae* protein database, and a database of common contaminant proteins
422 (including trypsin, keratin – found at ftp://ftp.thegpm.org/fasta/cRAP) with Thermo Proteome
423 Discoverer v 2.4.0.305 (Thermo Fisher Scientific). Fully tryptic peptides with up to 2 missed
424 cleavage sites were considered in MS/MS spectral matches. The variable modifications
425 considered included methionine oxidation (15.995 Da), cysteine carbamidomethylation (57.021
426 Da), and phosphorylation (79.966 Da) on serine, tyrosine, and threonine. XCorr score cutoffs at
427 95% confidence were used to identify proteins using a reverse database search[63]. Identification

428 results from proteins and peptides were further analyzed with Scaffold Q+S v 4.11.1 (Proteome
429 Software Inc., Portland OR), which integrates various search results (from Sequest, X!Tandem,
430 MASCOT) and using Bayesian statistics to identify spectra [64]. We considered protein identification
431 that satisfied the criteria of a minimum of two peptides with 95% confidence levels for protein and
432 peptide.

433

Limited proteolysis by trypsin protease

435 Fixed amounts of Lambda PP treated, and untreated Ycf1 protein (12 µg) sample were
436 incubated for 30 min on ice with trypsin from bovine pancrease (Sigma) at varying concentrations
437 (0, 0.5, 1, 2, 5, 10, and 15 µg/mL). The reaction was stopped by adding 1 µg/mL of soybean
438 trypsin inhibitor (Sigma) and incubating for an additional 15 min on ice. Next, 5 µL of each reaction
439 were mixed with 1X SDS loading dye and 100 mM DTT from each reaction and separated on a
440 10% SDS- PAGE gel before visualized with Coomassie Brilliant Blue R-250 staining.
441

References

1. Gueldry, O. *et al.* Ycf1p-dependent Hg(II) detoxification in Saccharomyces cerevisiae. *Eur. J. Biochem.* **270**, 2486–96 (2003).

2. Li, Z. S. *et al.* A new pathway for vacuolar cadmium sequestration in Saccharomyces cerevisiae: YCF1-catalyzed transport of bis(glutathionato)cadmium. *Proc. Natl. Acad. Sci. U. S. A.* **94**, 42–7 (1997).

3. Szczypka, M. S., Wemmie, J. A., Moye-Rowley, W. S. & Thiele, D. J. A yeast metal resistance protein similar to human cystic fibrosis transmembrane conductance regulator (CFTR) and multidrug resistance-associated protein. *J. Biol. Chem.* **269**, 22853–7 (1994).

4. Paumi, C. M., Pickin, K. A., Jarrar, R., Herren, C. K. & Cowley, S. T. Ycf1p attenuates basal level oxidative stress response in *Saccharomyces cerevisiae. FEBS Lett.* **586**, 847–853 (2012).

5. Morgan, B. *et al.* Multiple glutathione disulfide removal pathways mediate cytosolic redox homeostasis. *Nat. Chem. Biol.* **9**, 119–125 (2013).

6. I. Stolarczyk, E., J. Reiling, C. & M. Paumi, C. Regulation of ABC Transporter Function Via Phosphorylation by Protein Kinases. *Curr. Pharm. Biotechnol.* **12**, 621–635 (2011).

7. Szabó, K. *et al.* Phosphorylation site mutations in the human multidrug transporter modulate its drug-stimulated ATPase activity. *J. Biol. Chem.* **272**, 23165–23171 (1997).

8. Béguin, P., Nagashima, K., Nishimura, M., Gonoi, T. & Seino, S. PKA-mediated phosphorylation of the human K(ATP) channel: Separate roles of Kir6.2 and SUR1 subunit phosphorylation. *EMBO J.* **18**, 4722–4732 (1999).

9. Rich, D. P. *et al.* Regulation of the cystic fibrosis transmembrane conductance regulator Cl- channel by negative charge in the R domain. *J. Biol. Chem.* **268**, 20259–20267 (1993).

10. Pickin, K. A. *et al.* Suppression of Ycf1p function by Cka1p-dependent phosphorylation is attenuated in response to salt stress. *FEMS Yeast Res.* **10**, 839–857 (2010).

11. Eraso, P., Martínez-Burgos, M., Falcón-Pérez, J. M., Portillo, F. & Mazón, M. J. Ycf1-dependent cadmium detoxification by yeast requires phosphorylation of residues Ser 908 and Thr 911. *FEBS Lett.* **577**, 322–326 (2004).

12. Riordan, J. R. *et al.* Identification of the cystic fibrosis gene: Cloning and characterization of complementary DNA. *Science.* **245**, 1066–1073 (1989).

13. Ford, R. C., Marshall-Sabey, D. & Schuetz, J. Linker Domains: Why ABC Transporters 'Live in Fragments no Longer'. *Trends in Biochemical Sciences* **45**, 137–148 (2020).

14. Cheng, S. H. *et al.* Phosphorylation of the R domain by cAMP-dependent protein kinase regulates the CFTR chloride channel. *Cell* **66**, 1027–1036 (1991).

15. Mathews, C. J. *et al.* Dibasic protein kinase A sites regulate bursting rate and nucleotide sensitivity of the cystic fibrosis transmembrane conductance regulator chloride channel. *J. Physiol.* **508**, 365–377 (1998).

16. Paumi, C. M., Chuk, M., Chevelev, I., Stagljar, I. & Michaelis, S. Negative regulation of the yeast ABC transporter Ycf1p by phosphorylation within its N-terminal extension. *J. Biol. Chem.* **283**, 27079–27088 (2008).

17. Stolarczyk, E. I. *et al.* Casein kinase 2α regulates multidrug resistance-associated protein 1 function via phosphorylation of Thr249. *Mol. Pharmacol.* **82**, 488–499 (2012).

18. Bozoky, Z. *et al.* Regulatory R region of the CFTR chloride channel is a dynamic integrator of phospho-dependent intra- and intermolecular interactions. *Proc. Natl. Acad. Sci. U. S. A.* **110**, E4427-36 (2013).

19. Dulhanty, A. M. & Riordan, J. R. Phosphorylation by cAMP-Dependent Protein Kinase Causes a Conformational Change in the R Domain of the Cystic Fibrosis Transmembrane Conductance Regulator. *Biochemistry* **33**, 4072–4079 (1994).

20. Ostedgaard, L. S., Baldursson, O., Vermeer, D. W., Welsh, M. J. & Robertson, A. D. A

492   functional R domain from cystic fibrosis transmembrane conductance regulator is
493   predominantly unstructured in solution. *Proc. Natl. Acad. Sci. U. S. A.* **97**, 5657–5662
494   (2000).

495 21. Baker, J. M. R. *et al.* CFTR regulatory region interacts with NBD1 predominantly via
496   multiple transient helices. *Nat. Struct. Mol. Biol.* **14**, 738–745 (2007).

497 22. Johnson, Z. L. & Chen, J. Structural Basis of Substrate Recognition by the Multidrug
498   Resistance Protein MRP1. *Cell* **168**, 1075-1085.e9 (2017).

499 23. Zhang, Z., Liu, F. & Chen, J. Conformational Changes of CFTR upon Phosphorylation
500   and ATP Binding. *Cell* **170**, 483-491.e8 (2017).

501 24. Liu, F., Zhang, Z., Csanády, L., Gadsby, D. C. & Chen, J. Molecular Structure of the
502   Human CFTR Ion Channel. *Cell* **169**, 85-95.e8 (2017).

503 25. Zhang, Z., Liu, F. & Chen, J. Molecular structure of the ATP-bound, phosphorylated
504   human CFTR. *Proc. Natl. Acad. Sci. U. S. A.* **115**, 12757–12762 (2018).

505 26. Liu, F. *et al.* Molecular Structure of the Human CFTR Ion Channel. *Cell* **169**, 85–95
506   (2017).

507 27. Johnson, Z. L. & Chen, J. Structural Basis of Substrate Recognition by the Multidrug
508   Resistance Protein MRP1. *Cell* **168**, 1075-1085.e9 (2017).

509 28. Bickers, S. C., Benlekbir, S., Rubinstein, J. L. & Kanelis, V. Structure of Ycf1p reveals the
510   transmembrane domain TMD0 and the regulatory region of ABCC transporters. *Proc.*
511   *Natl. Acad. Sci.* **118**, e2025853118 (2021).

512 29. Morgan, B. *et al.* Multiple glutathione disulfide removal pathways mediate cytosolic redox
513   homeostasis. *Nat. Chem. Biol.* **9**, 119–125 (2013).

514 30. Marks, D. S., Hopf, T. A. & Sander, C. Protein structure prediction from sequence
515   variation. *Nature Biotechnology* **30**, 1072–1080 (2012).

516 31. Zheng, J. *et al.* 2.2 Å refined crystal structure of the catalytic subunit of cAMP-dependent
517   protein kinase complexed with MnATP and a peptide inhibitor. *Acta Crystallogr. Sect. D*
518   *Biol. Crystallogr.* **49**, 362–365 (1993).

519 32. Millan, C. R. *et al.* A Conserved Motif in Intracellular Loop 1 Stabilizes the Outward-
520   Facing Conformation of TmrAB. *J. Mol. Biol.* 166834 (2021).
521   doi:10.1016/j.jmb.2021.166834

522 33. Tommasini, R. *et al.* The human multidrug resistance-associated protein functionally
523   complements the yeast cadmium resistance factor. *Proc. Natl. Acad. Sci. U. S. A.* **93**,
524   6743–6748 (1996).

525 34. Zhang, Z., Liu, F. & Chen, J. Conformational Changes of CFTR upon Phosphorylation
526   and ATP Binding. *Cell* **170**, 483-491.e8 (2017).

527 35. Zhang, Z., Liu, F. & Chen, J. Molecular structure of the ATP-bound, phosphorylated
528   human CFTR. *Proc. Natl. Acad. Sci. U. S. A.* **115**, 12757–12762 (2018).

529 36. Naren, A. P. *et al.* CFTR chloride channel regulation by an interdomain interaction.
530   *Science.* **286**, 544–548 (1999).

531 37. Winter, M. C. & Welsh, M. J. Stimulation of CFTR activity by its phosphorylated R
532   domain. *Nature* **389**, 294–296 (1997).

533 38. Zhang, Z. & Chen, J. Atomic Structure of the Cystic Fibrosis Transmembrane
534   Conductance Regulator. *Cell* **167**, 1586-1597.e9 (2016).

535 39. Hudson, R. P. *et al.* Direct binding of the Corrector VX-809 to Human CFTR NBD1:
536   Evidence of an Allosteric coupling between the Binding site and the NBD1:CL4 Interface
537   s. *Mol. Pharmacol.* **92**, 124–135 (2017).

538 40. Dilworth, M. V *et al.* Microbial expression systems for membrane proteins. *Methods* **147**,
539   3–39 (2018).

540 41. Zivanov, J. *et al.* New tools for automated high-resolution cryo-EM structure
541   determination in RELION-3. *Elife* **7**, (2018).

542 42. Grant, T., Rohou, A. & Grigorieff, N. cisTEM, user-friendly software for single-particle

543   image processing. *Elife* **7**, (2018).

544   43.   Zheng, S. Q. *et al.* MotionCor2: anisotropic correction of beam-induced motion for
545   improved cryo-electron microscopy. *Nat. Methods* **14**, 331–332 (2017).

546   44.   Rohou, A. & Grigorieff, N. CTFFIND4: Fast and accurate defocus estimation from
547   electron micrographs. *J. Struct. Biol.* **192**, 216–221 (2015).

548   45.   Ramlaul, K., Palmer, C. M., Nakane, T. & Aylett, C. H. S. Mitigating local over-fitting
549   during single particle reconstruction with SIDESPLITTER. *J. Struct. Biol.* **211**, 107545
550   (2020).

551   46.   Kucukelbir, A., Sigworth, F. J. & Tagare, H. D. Quantifying the local resolution of cryo-EM
552   density maps. *Nat. Methods* **11**, 63–65 (2014).

553   47.   Waterhouse, A. *et al.* SWISS-MODEL: Homology modelling of protein structures and
554   complexes. *Nucleic Acids Res.* **46**, W296–W303 (2018).

555   48.   Ding, D., Wang, M., Wu, J. X., Kang, Y. & Chen, L. The Structural Basis for the Binding of
556   Repaglinide to the Pancreatic K ATP Channel. *Cell Rep.* **27**, 1848-1857.e4 (2019).

557   49.   Emsley, P. & Cowtan, K. Coot: Model-building tools for molecular graphics. *Acta
558   Crystallogr. Sect. D Biol. Crystallogr.* **60**, 2126–2132 (2004).

559   50.   Liebschner, D. *et al.* Macromolecular structure determination using X-rays, neutrons and
560   electrons: Recent developments in Phenix. *Acta Crystallogr. Sect. D Struct. Biol.* **75**,
561   861–877 (2019).

562   51.   Wood, C. *et al.* Collaborative computational project for electron cryo-microscopy. *Acta
563   Crystallogr. Sect. D Biol. Crystallogr.* **71**, 123–126 (2015).

564   52.   Murshudov, G. N. *et al.* REFMAC5 for the refinement of macromolecular crystal
565   structures. *Acta Crystallogr. Sect. D Biol. Crystallogr.* **67**, 355–367 (2011).

566   53.   Xu, D. & Zhang, Y. Improving the physical realism and structural accuracy of protein
567   models by a two-step atomic-level energy minimization. *Biophys. J.* **101**, 2525–2534
568   (2011).

569   54.   Croll, T. I. ISOLDE: A physically realistic environment for model building into low-
570   resolution electron-density maps. *Acta Crystallogr. Sect. D Struct. Biol.* **74**, 519–530
571   (2018).

572   55.   Williams, C. J. *et al.* MolProbity: More and better reference data for improved all-atom
573   structure validation. *Protein Sci.* **27**, 293–315 (2018).

574   56.   Voss, N. R. & Gerstein, M. 3V: Cavity, channel and cleft volume calculator and extractor.
575   *Nucleic Acids Res.* **38**, W555 (2010).

576   57.   Fan, C., Kaiser, J. T. & Rees, D. C. A structural framework for unidirectional transport by
577   a bacterial ABC exporter. *Proc. Natl. Acad. Sci. U. S. A.* **117**, 19228–19236 (2020).

578   58.   Eddy, S. R. Accelerated profile HMM searches. *PLoS Comput. Biol.* **7**, 1002195 (2011).

579   59.   Steinegger, M. *et al.* HH-suite3 for fast remote homology detection and deep protein
580   annotation. *BMC Bioinformatics* **20**, 473 (2019).

581   60.   Scharschmidt, B. F., Keeffe, E. B., Blankenship, N. M. & Ockner, R. K. Validation of a
582   recording spectrophotometric method for measurement of membrane-associated Mg-
583   and NaK-ATPase activity. *J. Lab. Clin. Med.* **93**, 790–799 (1979).

584   61.   Manolaridis, I. *et al.* Cryo-EM structures of a human ABCG2 mutant trapped in ATP-
585   bound and substrate-bound states. *Nature* **563**, 426–430 (2018).

586   62.   Andon, N. L. *et al.* Proteomic characterization of wheat amyloplasts using identification of
587   proteins by tandem mass spectrometry. *Proteomics* **2**, 1156–1168 (2002).

588   63.   Qian, W. J. *et al.* Probability-based evaluation of peptide and protein identifications from
589   tandem mass spectrometry and SEQUEST analysis: The human proteome. *J. Proteome
590   Res.* **4**, 53–62 (2005).

591   64.   Keller, A., Nesvizhskii, A. I., Kolker, E. & Aebersold, R. Empirical statistical model to
592   estimate the accuracy of peptide identifications made by MS/MS and database search.
593   *Anal. Chem.* **74**, 5383–5392 (2002).

612

613 **Author contributions:** Conceptualization: TM Tomasiak; Methodology: NKK, TM Thaker, TM
614 Tomasiak; Investigation: NKK, CRM, SZ, SA, DW, TM Thaker, TM Tomasiak; Visualization: NKK,
615 CRM, TM Thaker, TM Tomasiak; Funding acquisition: TM Tomasiak; Project administration: TM
616 Thaker, TM Tomasiak; Supervision: TM Tomasiak; Writing – original draft: NKK, TM Thaker, TM
617 Tomasiak; Writing – review & editing: NKK, CRM, TM Thaker, TM Tomasiak.

618

619 **Competing interests:** Authors declare that they have no competing interests

620

621 **Data and materials availability:** All data are available in the main text or the supplementary
622 materials. Structures presented here are available for download from the Protein Data Bank (PDB
623 codes: 7M68 and 7M69) and corresponding EM data from the EMDB (EMD-23690 and EMD-
624 23690, respectively).
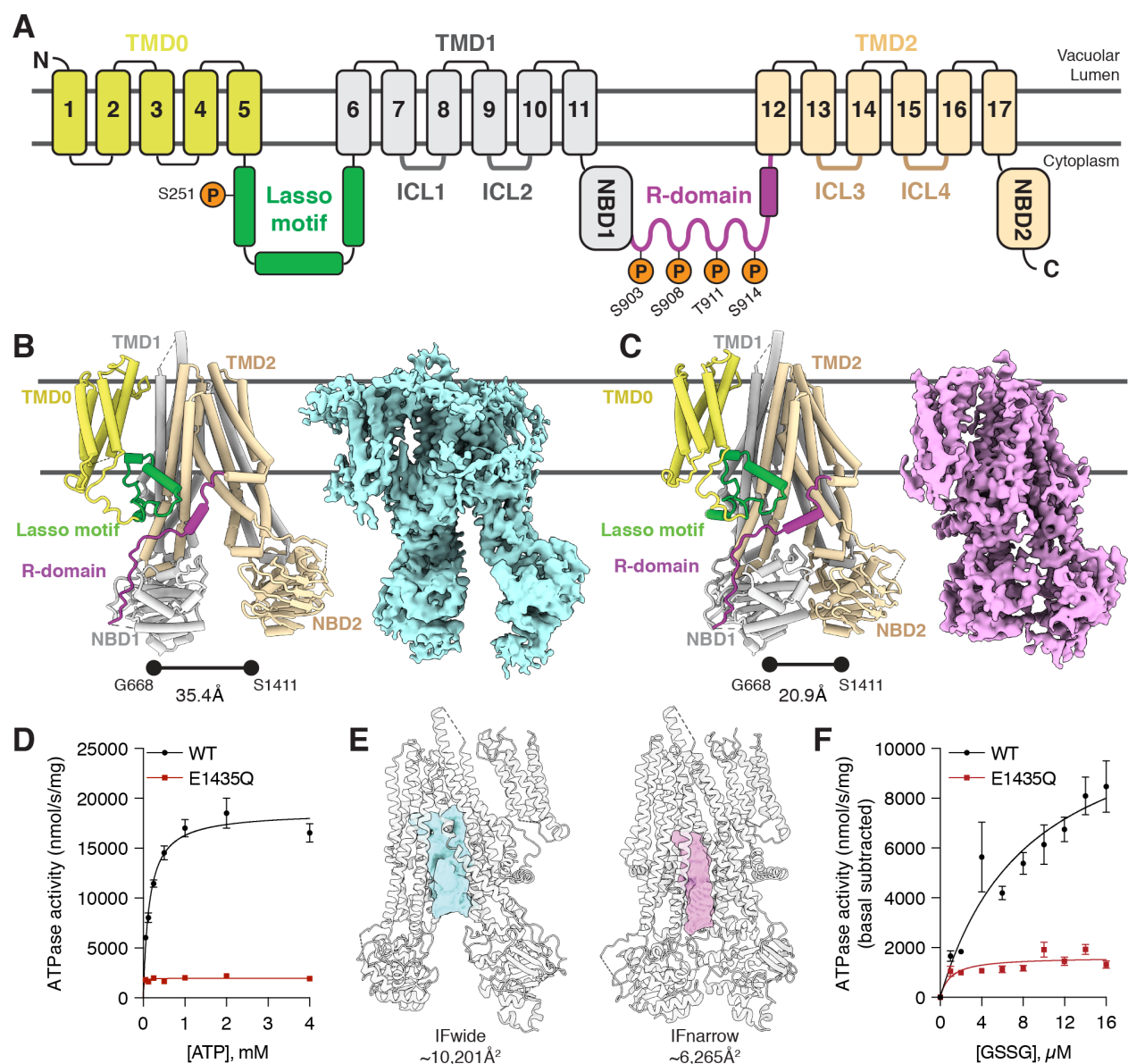
625   **Figures**
626
627   **Figure 1**

628

Fig. 1. The regulatory architecture of Ycf1 determined by cryo-EM. A. Schematic of Ycf1 structural topology highlighting the arrangement of transmembrane helices belonging to transmembrane domain 0 (TMD0, yellow), transmembrane domain 1 (TMD1, grey), and transmembrane domain 2 (TMD2, wheat). Conserved cytoplasmic elements shown include the lasso domain (green), the R-domain (purple), nucleotide binding domains 1 and 2 (NBD1 (grey); NBD2 (wheat)) and intracellular loops 1-4 (ICL1, ICL2 (dark grey); ICL3, ICL4 (brown)). Orange spheres corresponding to conserved putative phosphorylation sites in Ycf1 are labeled with their residue numbering on the corresponding domains. Cryo-EM model (left) and map (right) of the (**B**) IFwide (cyan) and (**C**) IFnarrow (pink) conformations of E1435Q Ycf1 colored using the same scheme as shown in (**A**). **D.** ATPase activity in the presence of increasing concentrations of ATP for wild-type (WT) and the catalytically dead (E1435Q) variant of Ycf1. **E**. Volume representation

640   of the internal cavities of IFwide (left, cyan) and IFnarrow (right, pink). **F.** ATPase activity in WT
641   and E1435Q Ycf1 in the presence of increasing concentrations of oxidized glutathione (GSSG)
642   and 1 mM ATP. Data are reported as stimulated rates in which the basal ATPase activity (without
643   GSSG) was subtracted. Data shown correspond to a half-maximal effective concentration (EC_{50})
644   of 8.67±2.6 µM for GSSG-induced stimulation of ATPase activity in WT Ycf1. Results in (**D**) and
645   (**F**) are the mean ± the standard deviation (S.D.) for n=3 (technical triplicates).

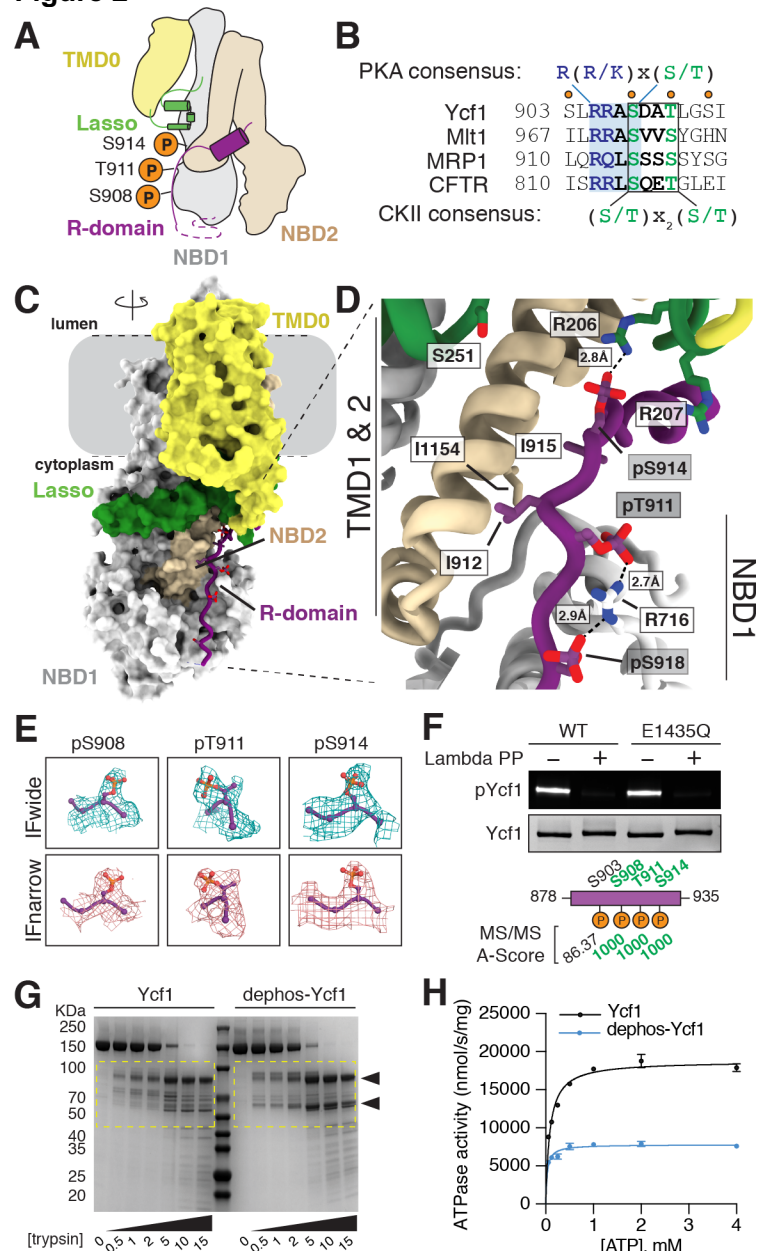646 **Figure 2**

647
648

649 **Fig. 2. The R-domain engages Ycf1 through an extensive phosphorylation-dependent**
650 **network. A.** Putative phosphorylation sites on the Ycf1 R-domain (purple) mapped onto a cartoon
651 representation of the Ycf1 IFnarrow cryo-EM structure. **B.** Sequence alignment of ABCC family
652 members highlighting the consensuses sequences of putative phosphorylation motifs. Orange
653 dots represent predicted phosphorylation sites. **C.** Surface representation of the cryo-EM model
654 of IFnarrow Ycf1 highlighting the orientation of the R-domain along NBD1. **D**. A detailed view of
655 the R-domain region shown in (**C**) highlighting residues contributing to the binding interface
656 between the R-domain (purple), the lasso domain (green), and NBD1 (grey). Carbon atoms are
657 colored consistent with domain coloring in (**C**), with oxygen (red), nitrogen (blue), and phosphate
658 (orange) atoms colored accordingly. Dashes represent hydrogen bonds or electrostatic
659 interactions between heavy atoms. **E.** Electron potential density of phosphorylated residues
660 (S908, T911 and S914) observed in IFwide (cyan) and IFnarrow (pink). **F.** SDS-PAGE analysis

661   of phosphorylation in purified samples of WT or the E1435Q variant of Ycf1 in the presence or
662   absence of Lambda phosphatase (Lambda PP) treatment. The top gel showing phosphorylated
663   Ycf1 (pYcf1) was stained with Pro-Q phosphoprotein gel stain (Thermo Fisher), whereas the
664   bottom gel was visualized with Coomassie gel stain to show total Ycf1 (Ycf1). Shown below the
665   gel are A-scores[63] for the LC-MS/MS experiment confirming the detection of phosphorylation at
666   the corresponding phosphorylation sites observed in the Ycf1 R-domain shown in (**D**) and
667   highlighted in (**A-E**). **G.** SDS-PAGE analysis of proteolysis resistance in Lambda PP untreated
668   (Ycf1) or treated (dephos-Ycf1) Ycf1 incubated with increasing concentrations of trypsin (0 – 15
669   µg/mL). **H.** ATPase activity of phosphorylated (Ycf1) and dephosphorylated (dephos-Ycf1). Data
670   shown are the mean ± S.D. for n=3 (technical triplicates).
671
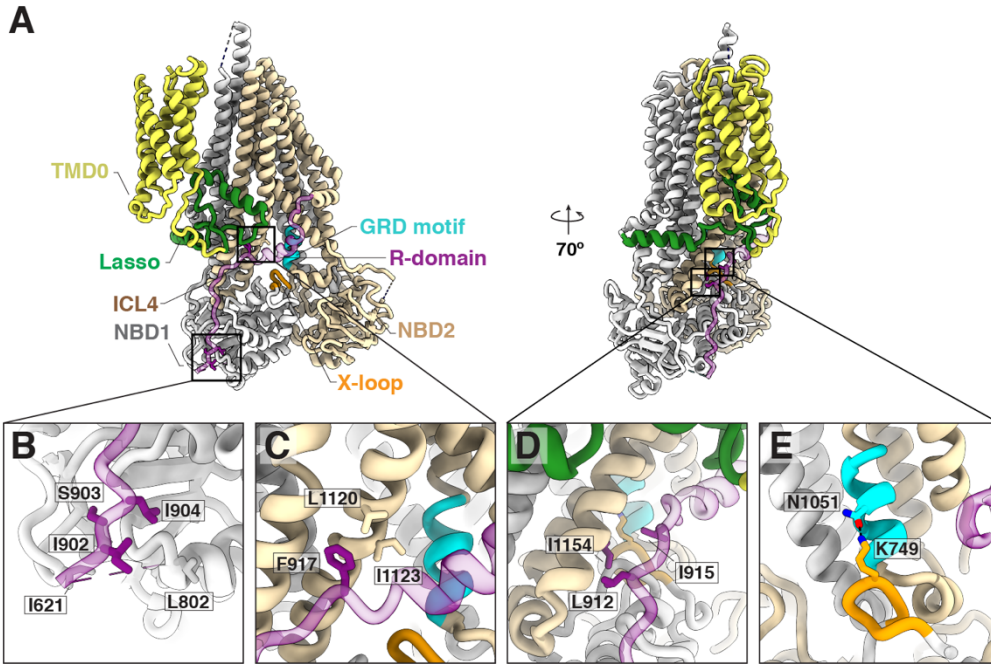
672   **Figure 3**

673

674

675

676   **Fig. 3. R-domain interaction network in Ycf1. A.** Overall structure of Ycf1 in IFnarrow. **B-D**.
677   Hydrophobic pockets along the R-domain/NBD interface. **E**. Interactions between residues of the
678   X-loop and GRD motif in IFnarrow. The R-domain is colored purple, TMD1-NBD1 is colored grey,
679   TMD2 and NBD2 are colored wheat, lasso domain is colored green, the X-loop is colored orange,
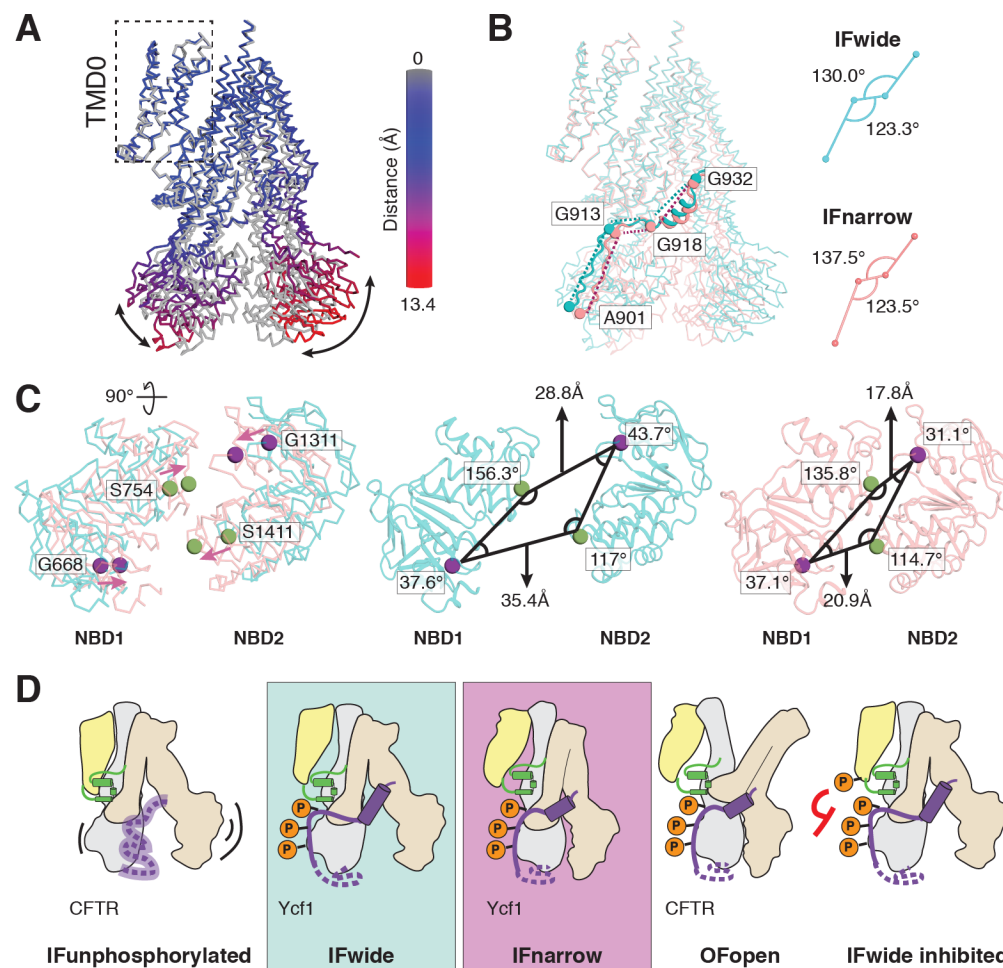680   and the GRD motif is colored cyan in all figures.

681   **Figure 4**
682

683

684   **Fig. 4. Proposed model for catalytic control in Ycf1 relies on transitions of the rigid R-**
685   **domain architecture from IFwide to IFnarrow. A.** Overlay of IFnarrow (grey) and IFwide states
686   of Ycf1, in which IFwide is colored by RMSD calculated on a per residue basis from structural
687   alignment between TMD0 of each state. **B.** Comparison of the R-domain geometry and
688   differences observed for the intradomain angles between flexible residues forming hinge regions
689   in the R-domains in each state. **C.** Superposed NBDs (left panel) from IFwide (cyan ribbon) and
690   IFnarrow (pink ribbon) highlighting the rearrangement in the relative positions of conserved
691   residues of the signature motif (S754 and S1411, green sphere) and the walker A motif (G668
692   and G1311, purple spheres) in each state. The specific interdomain angles formed by these sites
693   in their respective states are shown in the middle (IFwide) and right (IFnarrow) panels. **D.**
694   Proposed model for organization and regulation of the R-domain through transport in light of the
695   IFwide and IFnarrow Ycf1 structures and in the context of previously published CFTR structures
696   (IFunphosphorylated (PDB ID 5uak[26]); OFopen (PDB ID 6msm[25]). Domains are colored yellow
697   for TMD0, gray for TMD1 and NBD1, wheat for TMD2 and NBD2, green for the Lasso domain,
698   and purple for the R-domain.